MDPI

Article

Simultaneous Dual-Modal Multispectral Photoacoustic and Ultrasound Macroscopy for Three-Dimensional Whole-Body Imaging of Small Animals

Eun-Yeong Park [1,†], Sinyoung Park [1,†], Haeni Lee [2], Munsik Kang [2], Chulhong Kim [1,*] and Jeesu Kim [2,*]

[1] Departments of Electrical Engineering, Creative IT Engineering, Mechanical Engineering, and Medical Device Innovation Center, Pohang University of Science and Technology (POSTECH), Gyeongbuk 37673, Korea; pey0531@postech.ac.kr (E.-Y.P.); sinyoungpark@postech.ac.kr (S.P.)

[2] Department of Cogno-Mechatronics Engineering, College of Nanoscience & Nanotechnology, Pusan National University, Busan 46241, Korea; dovelet2@pusan.ac.kr (H.L.); dkswo4168@pusan.ac.kr (M.K.)

[*] Correspondence: chulhong@postech.edu (C.K.); jeesukim@pusan.ac.kr (J.K.)

[†] These authors contributed equally to this work.

Abstract: Photoacoustic imaging is a promising medical imaging technique that provides excellent function imaging of an underlying biological tissue or organ. However, it is limited in providing structural information compared to other imaging modalities, such as ultrasound imaging. Thus, to offer complete morphological details of biological tissues, photoacoustic imaging is typically integrated with ultrasound imaging. This dual-modal imaging technique is already implemented on commercial clinical ultrasound imaging platforms. However, commercial platforms suffer from limited elevation resolution compared to the lateral and axial resolution. We have successfully developed a dual-modal photoacoustic and ultrasound imaging to address these limitations, specifically targeting animal studies. The system can acquire whole-body images of mice in vivo and provide complementary structural and functional information of biological tissue information simultaneously. The color-coded depth information can be readily obtained in photoacoustic images using complementary information from ultrasound images. The system can be used for several biomedical applications, including drug delivery, biodistribution assessment, and agent testing.

Keywords: photoacoustic imaging; ultrasound imaging; dual-modal imaging; whole-body imaging; 3D imaging

1. Introduction

Photoacoustic (PA) imaging is a biomedical imaging technique widely used in various preclinical and clinical studies. The principle of PA imaging is based on the PA effect, which is the energy transduction from light to acoustic pressure wave [1,2]. The optical absorption at the target tissue generates broadband ultrasound (US) waves called PA waves, which are recorded using conventional piezoelectric US transducers. Since the PA waves are generated by thermoelastic expansion and contraction of tissues, the captured PA signals reflect biological tissue optical absorption properties. As compared to conventional optical imaging techniques, the PA signals are much less scattered in biological tissue than optical beam [3], thus providing strong optical contrasts with high US resolution in deep tissue [4–6]. The contrast in PA images can be further enhanced by using optically absorbing exogenous and endogenous contrast agents [5,7]. For exploiting the advantage of PA imaging in biomedical studies, various types of PA imaging instruments have already been developed and applied [8–13].

For clinical use, PA imaging and US imaging have been integrated into one platform since the signal reception, and image reconstruction methods of the two platforms are similar and share the single data acquisition system [14–20]. In addition, US imaging is widely used for clinical diagnosis, making the integrated system more favorable for clinical

translation. The combined approach provides complementary information (i.e., anatomical information from US images and functional optical absorption characteristics from PA images), facilitating clinical diagnosis and therapeutic monitoring [21–24]. In addition, the PA image quality can be enhanced by US image aided skin-signal removal [25].

Dual-modal PA and US imaging has already been used in many preclinical studies [26–30]. The commercial preclinical PA and US imaging machine (Vevo LAZR series, Fujifilm VisualSonics, Toronto, ON, Canada) has been utilized for in vivo imaging of small animals [31–35]. The system provides real-time US and PA imaging with tunable wavelength using a linear-array transducer. Its intuitive user interface and mobility make the user easily acquire PA and US images. The linear-array transducer enables real-time B-mode imaging but is limited for 3D imaging due to limited elevation resolution compared to the lateral and axial resolution. The low elevational resolution degrades the image quality when the 3D data are projected onto the 2D transversal plane, which is a widely used technique for visualizing 3D blood vessel networks for monitoring the biodistribution of contrast agents. In addition, the lateral field of view (FOV) of the system is limited by the width of the transducer, which is typically ~30–40 mm, because the volumetric images are typically achieved by motorized scanning of linear-array transducer (Figure S1a).

Compared to the array-based transducer, dual-modal PA and US imaging system with a spherical single-element transducer still have advantages for some applications that do not require real-time imaging. The spherical single-element transducer also has an advantage of equivalent lateral and elevational resolutions. In addition, because the volumetric data are typically achieved from a raster scanning of the single-element transducer, the lateral FOV can be enlarged (Figure S1b). Harrison et al. reported a combined PA and US imaging system equipping a 25 MHz focused transducer [36]. The performance of the system was validated with in vitro and in vivo experiments. However, the system was not fully integrated since the PA and US images were not acquired simultaneously. Recently, Wang et al. demonstrated an integrated detector for PA and US imaging and validated their system for melanoma detection in vivo [37]. The system acquired 3D images of PA and US from melanoma and generated landscape images to visualize the blood vessel network and the regions surrounding it. However, this system only uses a single wavelength (532 nm) for imaging.
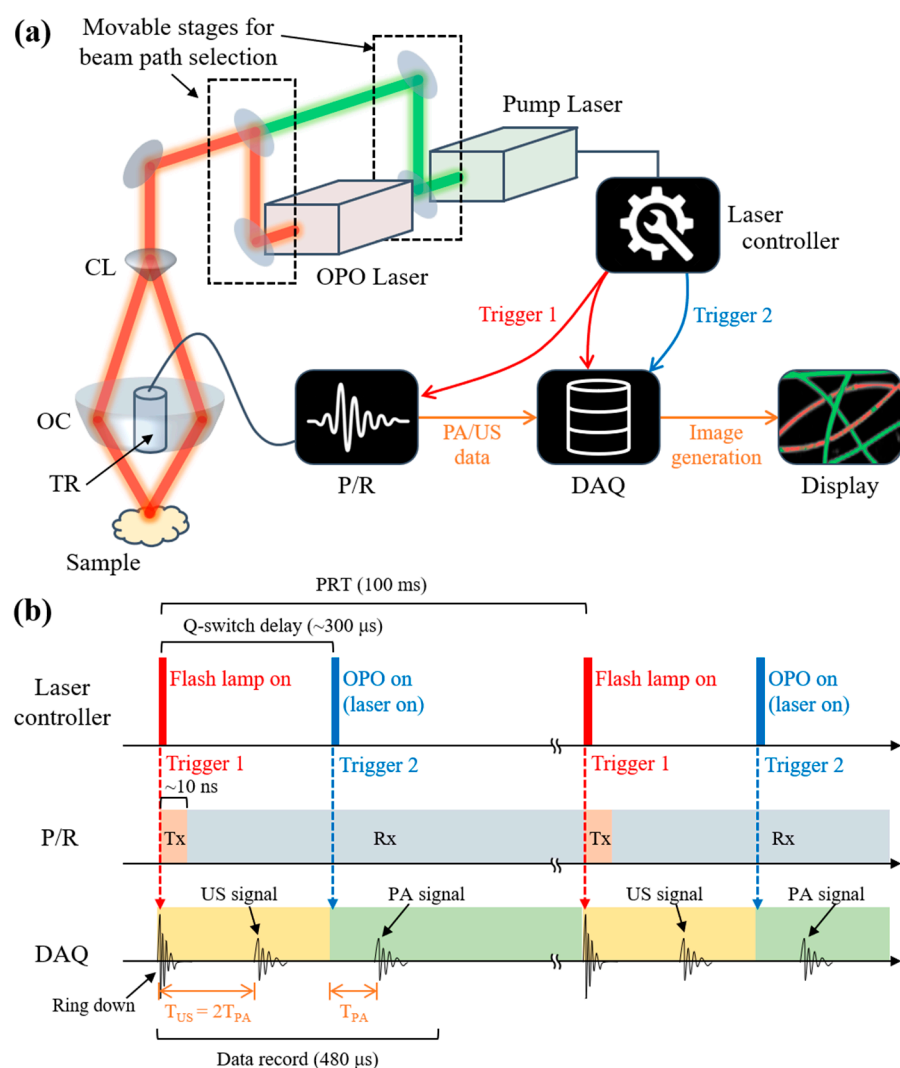
Here, we present a dual-modal PA and US imaging system using a spherical single-element transducer. The new system advances the previously reported system and can acquire multispectral whole-body images of small animals in vivo [38]. The system can acquire PA and US images simultaneously and provide structural and functional information of the target. We benchmarked the performance of the system using in vitro phantoms and in vivo mice. The results show the potential of our system for various biomedical imaging studies.

2. Materials and Methods

2.1. Dual-Modal Photoacoustic and Ultrasound Imaging System

To implement a dual-modal PA and US imaging system, we modified the previously reported PA imaging system (Figure 1a) [38]. The system consists of mainly three parts: (1) laser source, (2) laser delivery optics, and (3) data acquisition and image generation module. Two laser modules generate a different range of wavelengths: (1) a Q-switched pump laser (Surelite III-10, Continuum, USA), which generates single wavelength lasers of 532 or 1064 nm, and (2) an optical parametric oscillator (OPO) laser (Surelite OPO PLUS, Continuum, USA), which produces tunable wavelength with the range from 690 to 930 nm. The two light paths can be switched by using movable stages (dashed rectangles in Figure 1a). Optical mirrors and lens are used to deliver light to the sample stage. The conical lens diverts the light to bypass the US transducer, and the optical condenser merges the light back into the sample. The laser controller sends triggers to the pulser/receiver (P/R) and data acquisition (DAQ) module to synchronize them. The PA and US waves are detected by the 5 MHz US transducer (V308, Olympus NDT, Waltham MA USA) with

a -6 dB bandwidth of 100%. The received signals are amplified by the P/R (5072PR, Olympus NDT, Waltham MA USA) and stored by the DAQ module (MSO 5204, Tektronix, Beaverton OR USA). The stored data are processed to generate images with a custom made image processing software, which was developed based on the Matlab (R2020b, Mathworks, Natick MA USA) development environment. We used two triggers for acquiring PA and US data simultaneously, as shown in Figure 1b. For the Q-switched pump laser, a small time-difference (i.e., Q-switch delay) exists between the flash lamp and actual laser illumination. The typical Q-switch delay is ~300 µs, sufficient for US pulse–echo imaging in small animals. Once the flash-lamp trigger is detected, the P/R transmits US pulses, and the DAQ module begins to record the data for 480 µs. First, the reflected US signals are detected, then after the second trigger, generated PA signals are detected. The DAQ stores both trigger information to calculate the time of flight for PA and US signals.

Figure 1. Schematic illustration of the dual-modal PA and US imaging system. (**a**) Configuration of the system. (**b**) The operation sequence of the system for simultaneous dual-modal imaging. PA, photoacoustic; US, ultrasound; TR, transducer; OC, optical condenser; CL, conical lens; OPO, optical parametric oscillator; P/R, pulser-receiver; DAQ, data acquisition module; PRT, pulse repetition time; Tx, transmission; Rx, reception; T_{US}, flight time of ultrasound signal; T_{PA}, flight time of the photoacoustic signal.

2.2. Resolution Test

A ~120 μm thick human hair target, measured by a digital microscope (AM73515MZTL, Dino-Lite, Torrance, CA USA), was prepared to measure the spatial resolution of the system. The hair target was fixed on a custom-designed acrylic holder with a silicone sealant (KE-441, Shin-Etsu, Japan) and immersed into the water tank. The immersed target was scanned using our system, acquiring both PA and US images. The total scanning area was 20×10 mm^2 with the step sizes of 0.2 mm (stepped the transducer using the movable stages) in both X and Y directions. An optical wavelength of 700 nm with a fluence of 9 mJ/cm^2 was used to acquire PA images of the hair.

2.3. Blood Vessel Mimicking Phantom

For mimicking blood vessels, red and green tubes are prepared by filling silicone tubes (508-001, Dow Corning, Midland, MI, USA) with the gelatin mixture of light-absorbing inks (Fiesta red and Ebony green, Private Reserve Ink, USA). The inner and outer diameters of the silicone tubes were 0.30 and 0.64 mm, respectively. The gelatin mixture was prepared by dissolving 1 g of gelatin (G2500, Sigma-Aldrich, St. Louis, MO, USA) in 20 mL of water and then adding 100 μL of inks. Before the solutions were solidified, jellylike solutions were injected into the silicone tubes using 26 gauge syringes. Once the gelatin mixtures in the silicone tubes were solidified, the tubes were placed in the middle of a cuboid gelatin phantom, which composed 10 g of gelatin in 100 mL of water. To prepare the cuboid phantom, we first made the bottom half of the cuboid, placed the dyed tubes, and then poured the gelatin solution over the cuboid to form the cuboid's top half. The phantom was left for solidifying over 24 h. The finished phantom was submerged into the water tank for acquiring PA and US data images. The scanning area was 30×20 mm^2 with step sizes of 0.2 and 0.5 mm in the X and Y direction, respectively. For spectral analysis, PA images were acquired at two optical wavelengths of 532 and 700 nm with the corresponding fluences of 9 and 4 mJ/cm^2, respectively.

2.4. Animal Imaging Protocol

All experimental animal procedures were performed following the protocol approved by the institutional animal care and use committee of the Pohang University of Science and Technology (POSTECH-2020-0071-C1). A healthy one 9-week-old BALB/c nude mouse (~20 g) was prepared to acquire PA and US images. A vaporized isoflurane system (1 L/min of oxygen and 0.75% isoflurane) was used to anesthetize the mouse during the experiment. The hair of the mouse in the imaging region was removed carefully using a depilatory cream. The mouse was placed under the water tank, with the conventional ultrasound gel (Ecosonic, SANIPIA, Republic of Korea) applied between the membrane and mouse skin. The raster scanning area was 60×40 mm^2 with the step sizes 0.2 and 0.5 mm in the X and Y direction, respectively. The total data acquisition time for one volumetric image was ~30 min, which was limited by the laser repetition rate of 10 Hz. The multispectral PA and corresponding US images were acquired at 700, 800, and 900 nm wavelengths, with the fluences of 4, 4, and 3 mJ/cm^2, respectively. After the image acquisition, the mouse was sacrificed by overdosing with carbon dioxide, and the position of organs was verified by removing skin tissues.

3. Results and Discussion

3.1. Spatial Resolution

To validate the spatial resolution of the system, we acquired volumetric data of both PA and US of human hair phantom in a single scanning process (Figure 2a). The maximum amplitude projection (MAP) images were then generated from the acquired 3D volume data, using the Matlab-based custom image processing software for measuring the spatial resolution. We evaluated lateral and axial profiles of both PA and US images by analyzing the data points. At the maximum value of each cross-sectional image (Figure 2b), the lateral and axial resolutions were quantified by measuring the full width at half maximum

(FWHM) of the Gaussian fitted line (Figure 2c). We averaged the FWHM values of all the 100 scan lines (X scans, 20 mm scanning with 0.2 mm step in the Y direction). The measured lateral and axial resolutions of PA images are 1.16 ± 0.04 and 0.32 ± 0.04 mm (mean $\pm$ standard deviation), respectively, while those of US images are 0.76 ± 0.07 and 0.38 ± 0.03 mm, respectively. Since the frequency range of the acoustic waves is identical for both images, which determines the system's axial resolution, the axial resolution of PA and US images is also similar. The experimental result matches well with the theoretical axial resolution of 0.31 mm. The lateral resolutions of the PA and US images, however, are different from one another. In the US imaging, the lateral resolution is best at the focal zone, where most of the ultrasound energy is focused. The obtained lateral resolution of 0.76 ± 0.07 mm at the focal zone matches the theoretical value of 0.61 mm. The PA waves, however, are generated throughout the imaging plane. Those PA waves propagate in all directions and are detected by the transducer. Thus, the PA waves' lateral resolution (1.16 ± 0.04) is lower than US images' resolution $(0.76 \pm 0.07$ mm).
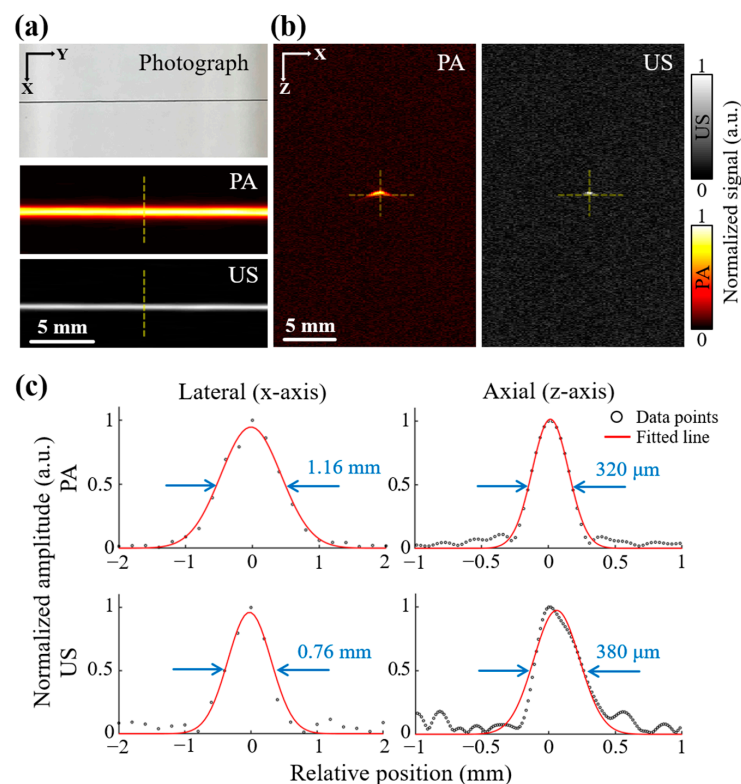

Figure 2. Performance benchmark of the PA and US imaging system. (**a**) Photograph, PA MAP, and US MAP images of the resolution phantom. The scale bars are equal for X and Y directions. (**b**) Cross-sectional PA and US images correspond to yellow dashed lines in (A). The scale bars are equal for X and Z directions. (**c**) Data points and Gaussian fitted lines along the lateral and axial direction. Resolutions are calculated as the full width at half maximum of each fitted line. Based on the geometry of the US transducer, the theoretical lateral and axial resolutions are 610 and 310 μm, respectively. PA, photoacoustic; US, ultrasound; MAP, maximum amplitude projection.

To evaluate the capability of the system with the enhanced elevational resolution compared to the conventional linear-array-based imaging system, we acquired volumetric data of the resolution target by using the previously reported PA and US imaging system [14]. We scanned the resolution phantom in the elevational direction with a step size of 0.2 mm (Figure S2a). The resulting images show the lower resolution in the linear-array system (Figure S2b). The measured elevational resolutions of photoacoustic and ultrasound imaging are 4.25 ± 0.08 and 2.19 ± 0.08 mm, respectively. Compared to the linear-array system,

the proposed system has enhanced elevational resolutions in both PA (1.16 $\pm$ 0.04 mm) and US (0.76 $\pm$ 0.07 mm) imaging. We can note that the lateral and elevational resolutions of the single-element system are identical because the spherical single-element the transducer has an equivalent focal spot in lateral and elevational directions. From the results, we can conclude that the proposed system could have an advantage for visualizing transversal MAP images compared to the linear-array-based system with equivalent lateral and elevational resolutions.

### 3.2. Photoacoustic and Ultrasound Images of Blood Vessel Mimicking Phantom

To verify the system's dual-modal imaging capability, we acquired PA and US images of the blood vessel mimicking phantom (Figure 3a). The acquired US and PA images are shown in Figure 3b–d. The US image is in gray-scale while the PA images are in pseudo-color. For better visualization of the tubular network, transverse MAP images are acquired. The US images show the structural information of tubes but cannot differentiate between two types of tubes. In contrast, the red and green tubes are differentiable in PA images since they have different optical absorption spectra. The average amplitudes of the two tubes are shown in Figure 3e. The plot shows that the red tube's PA amplitude decreases with increasing wavelength, while that of the green tube is maintained. The spectral response of two tubes depicting red and green tube images are overlaid on corresponding US images (Figure 3f–h). The overlaid images delineate the red and green tubes with different color-codes. These results confirm that our system can distinguish different chromophores by analyzing multispectral PA and US images.
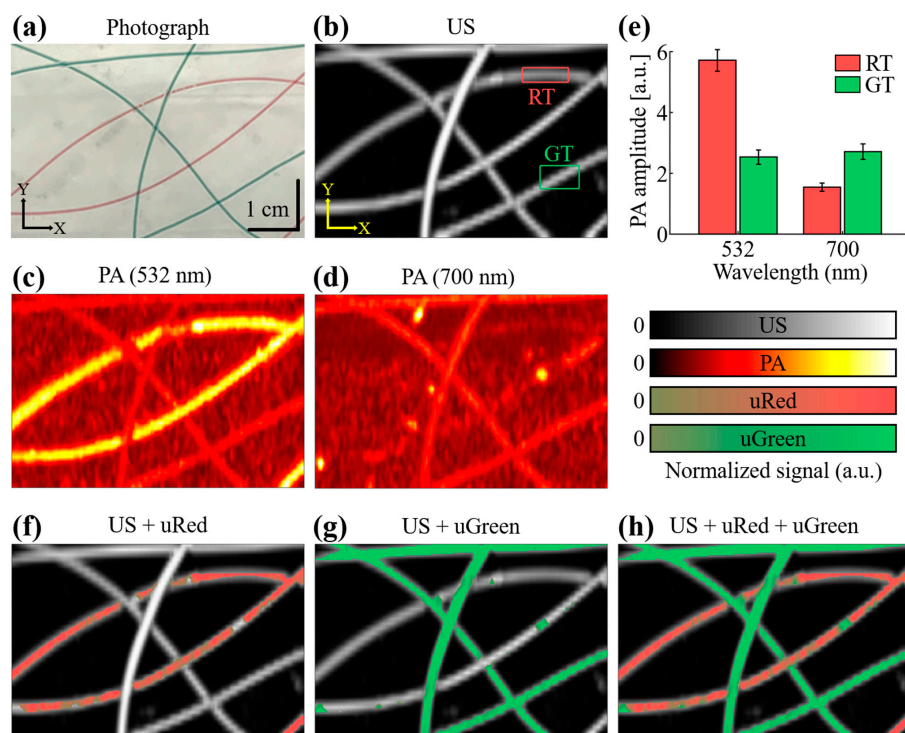
Figure 3. In vitro imaging of the blood vessel mimicking phantom. (**a**) Photograph of the phantom. (**b**) US MAP image of the phantom. Red and green rectangular indicate the ROI of the RT and GT for quantification. (**c**,**d**) Normalized PA MAP images of the phantom with the excitation wavelength of 532 and 700 nm. (**e**) Quantified PA amplitudes of the RT and GT. (**f**–**h**) Overlaid MAP images of the phantom with unmixed PA MAP images over the US MAP image. PA, photoacoustic; US, ultrasound; MAP, maximum amplitude projection; RT, red tube; GT, green tube; uRed, unmixed red; uGreen, unmixed green.

3.3. Whole-Body Photoacoustic and Ultrasound Images of Small Animals In Vivo

For in vivo validation, volumetric PA and US images of a mouse were acquired using multiple wavelengths (i.e., 700, 800, and 900 nm). The photographs of mice before and after the experiment are shown in Figure 4a,b. Like the phantom images above, the US images provide structural information of internal organs (i.e., body boundary, ribs, and bones) and gauzes, which were used to level the mouse body (Figure 4c). The overlaid PA and US B-mode images show both structures (from US image) and optical absorption characteristics (from PA images) of internal organs (Figure 4d–f). All the US images are in gray-scale color, while PA images are depicted in pseudo-red color. The position and structure of internal organs (i.e., spleen, liver, and intestine) and major blood vessels in PA images are revealed when MAP is used (Figure 4g–i).
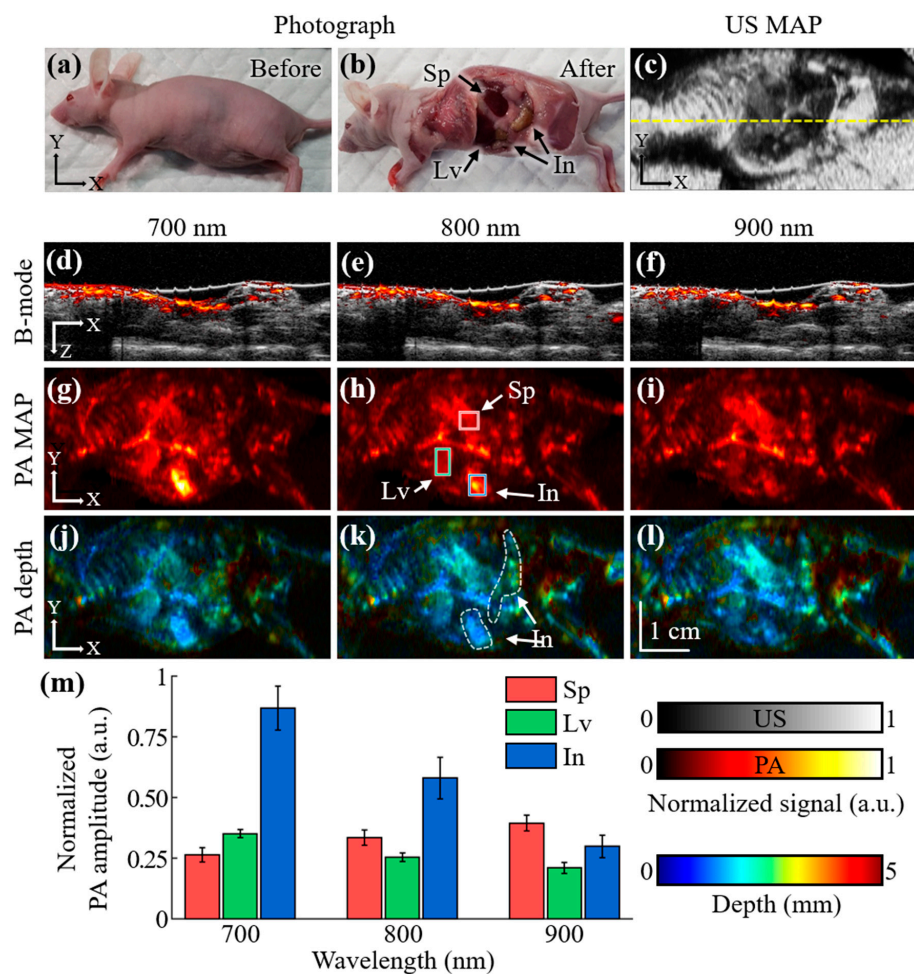
Figure 4. In vivo whole-body imaging of a mouse. (**a**,**b**) Photograph of the mouse before and after experiments. (**c**) US MAP images of the mouse after removing membrane signals. (**d**–**f**) Overlaid B-mode images of the mouse at the cross-sectional plane indicated as the yellow dashed line in (**c**). (**g**–**i**) PA MAP images of the mouse with excitation wavelengths of 700, 800, and 900 nm. (**j**–**l**) Depth-coded PA MAP images of the mouse. The white dashed lines represent the intestine at deep tissue, revealed with the depth-coded PA images. The depth of each pixel is calculated as the distance from the skin, which is determined from the corresponding US images. (**m**) Quantified PA signals at the ROIs depicted as colored rectangles in (**h**). Same ROIs are applied to the PA MAP images at each excitation wavelength. PA, photoacoustic; US, ultrasound; MAP, maximum amplitude projection; ROI, region of interest; Sp, spleen; In, intestine; Lv, liver.

We also visualized 3D volumes of both PA and US images (Figure S1, Movies S1–S3) by using the previously developed and reported 3D rendering software (3D PHOVIS) [39]. In the rendered image, we can see that the blood vessels are visible only in PA images because of the strong optical absorption of hemoglobin. The position of organs in the US and PA images are verified in the photograph taken after the experiment (Figure 4b). In addition, since the position of the skin layer can be delineated in US images, the distance between the signal and skin layer can be easily calculated. Previous studies, however, were limited to represent depth-coded PA images for several reasons: (1) they assumed skin is flat, which is not true in most cases, (2) they manually assigned the skin layers, subjecting to operator variability, or (3) they modeled the surface as a sphere, which applies to eyes only. In this study, as previously mentioned, the PA signal's depth is successfully calculated by measuring the distance between the signal location in the PA images and the skin layer in the corresponding US images (Figure 4j–l). All the quantification is performed using a custom-designed image processing software with graphical interfaces (Figure S2) based on the Matlab (R2020b, Mathworks, USA). The depth-coded PA images provide depth information of PA MAP images using a pseudo-color code (blue indicates shallow, red indicates deep signals). From the accurate depth-coded PA images, more information can be derived. For instance, the intestine in deep tissue is revealed clearly in the depth-coded PA images (white dashed lines in Figure 4k) compared to PA MAP images (Figure 4g–i, where it is difficult to distinguish.

The signal amplitudes in PA images depend upon the optical absorption characteristic of biological tissue and thus vary with the excitation wavelength. For investigating the signal difference between different wavelengths, we first determined the region of interest (ROI) to be evaluated for each major organ. The ROI is depicted in Figure 4h as red, green, and blue rectangles for the spleen, liver, and intestine. The top 30% of PA amplitudes in each ROI are extracted and averaged for quantification (Figure 4m). At the longer wavelength, the spleen's PA amplitudes decrease while those for the liver and intestine increases. These results match well with the previously reported article, thus confirming our findings [38].

4. Conclusions

In this study, we have successfully presented a dual-modal PA and US imaging system that can acquire whole-body images of mice in vivo. We demonstrated the visualization of multispectral PA images with the corresponding US images with a single simultaneous scanning procedure. With the multispectral analysis, the system could distinguish the chromophores with different optical absorption spectra. The PA images depict optical absorption characteristics of internal organs and blood vessels, while the US images delineate the boundaries, bones, and skin surface. From the skin position information, the signal depth of the PA MAP images can be assessed accurately. Compared to the previous depth encoded PA imaging approaches, our method is accurate and fully automated. We also visualized in vivo volumetric whole-body images of mice at different wavelengths. The results showed the relationship between the image amplitude to the excitation wavelength for visualizing both structural and functional information of biological tissue. Although the image acquisition of the system is slower than the commercial linear-array-based systems, the proposed system has advantages for some applications, including (1) preclinical experiments that do not require real-time imaging, (2) in vitro experiments for assessing PA and US response of agents, (3) experiments that require equivalent spatial resolution. At this time, we used a 5 MHz transducer to achieve whole-body images. Image analysis with other frequency bandwidth would improve the capability of the system. Because we can easily replace the transducer in the system, we can choose the proper transducer based on the target imaging depth and resolution.

The achieved depth range (i.e., 0–5 mm) and measured spatial resolution (i.e., 1.18 ± 0.08 mm) of PA imaging are good enough for the expected applications of the proposed system. We expect the main application of the system would be preclinical experiments that require whole-body biodistribution of mice such as, monitoring of drug delivery, tumor growth, metastasis, or treatment. Thus, we believe our method is advantageous for various biomedical small animal studies and provides both PA and US images in vivo simultaneously.

References

1. Bell, A.G. The photophone. *Science* **1880**, *1*, 130–131. [CrossRef] [PubMed]
2. Kim, C.; Favazza, C.; Wang, L.V. In Vivo Photoacoustic Tomography of Chemicals: High-Resolution Functional and Molecular Optical Imaging at New Depths. *Chem. Rev.* **2010**, *110*, 2756–2782. [CrossRef] [PubMed]
3. Chitgupi, U.; Nyayapathi, N.; Kim, J.; Wang, D.; Sun, B.; Li, C.; Carter, K.; Huang, W.C.; Kim, C.; Xia, J. Surfactant-Stripped Micelles for NIR-II Photoacoustic Imaging through 12 cm of Breast Tissue and Whole Human Breasts. *Adv. Mater.* **2019**, *31*, 1902279. [CrossRef] [PubMed]
4. Kim, J.; Park, S.; Lee, C.; Kim, J.Y.; Kim, C. Organic Nanostructures for Photoacoustic Imaging. *ChemNanoMat* **2015**, *2*, 156–166. [CrossRef]
5. Lee, C.; Kim, J.; Zhang, Y.; Jeon, M.; Liu, C.; Song, L.; Lovell, J.F.; Kim, C. Dual-color photoacoustic lymph node imaging using nanoformulated naphthalocyanines. *Biomaterials* **2015**, *73*, 142–148. [CrossRef]
6. Jung, H.; Park, S.; Gunassekaran, G.R.; Jeon, M.; Cho, Y.-E.; Baek, M.-C.; Park, J.Y.; Shim, G.; Oh, Y.-K.; Kim, I.-S.; et al. A Peptide Probe Enables Pphotoacoustic-Guided Imaging and Drug Delivery to Lung Tumors in K-rasLA2 Mutant Mice. *Cancer Res.* **2019**, *79*, 4271–4282. [CrossRef]

7. Zhang, Y.; Jeon, M.; Rich, L.J.; Hong, H.; Geng, J.; Zhang, Y.; Shi, S.; Barnhart, T.E.; Alexandridis, P.; Huizinga, J.D. Non-Invasive Multimodal Functional Imaging of the Intestine with Frozen Micellar Naphthalocyanines. *Nat. Nanotechnol.* **2014**, *9*, 631–638. [CrossRef]

8. Jeon, S.; Kim, J.; Lee, D.; Woo, B.J.; Kim, C. Review on practical photoacoustic microscopy. *Photoacoustics* **2019**, *15*, 100141. [CrossRef]

9. Kim, J.; Kim, J.Y.; Jeon, S.; Baik, J.W.; Cho, S.H.; Kim, C. Super-resolution localization photoacoustic microscopy using intrinsic red blood cells as contrast absorbers. *Light Sci. Appl.* **2019**, *8*, 1–11. [CrossRef]

10. Jeon, S.; Song, H.B.; Kim, J.; Lee, B.J.; Managuli, R.; Kim, J.H.; Kim, J.H.; Kim, C. In vivo photoacoustic imaging of anterior ocular vasculature: A random sample consensus approach. *Sci. Rep.* **2017**, *7*, 1–9.

11. Park, E.-Y.; Lee, D.; Lee, C.; Kim, C. Non-Ionizing Label-Free Photoacoustic Imaging of Bones. *IEEE Access* **2020**, *8*, 160915–160920. [CrossRef]

12. Upputuri, P.K.; Pramanik, M. Performance characterization of low-cost, high-speed, portable pulsed laser diode photoacoustic tomography (PLD-PAT) system. *Biomed. Opt. Express* **2015**, *6*, 4118–4129. [CrossRef] [PubMed]

13. Upputuri, P.K.; Pramanik, M. Dynamic in vivo imaging of small animal brain using pulsed laser diode-based photoacoustic tomography system. *J. Biomed. Opt.* **2017**, *22*, 090501. [CrossRef] [PubMed]

14. Kim, J.; Park, S.; Jung, Y.; Chang, S.; Park, J.; Zhang, Y.; Lovell, J.F.; Kim, C. Programmable Real-time Clinical Photoacoustic and Ultrasound Imaging System. *Sci. Rep.* **2016**, *6*, 35137. [CrossRef] [PubMed]

15. Kim, J.; Park, E.-Y.; Park, B.; Choi, W.; Lee, K.J.; Kim, C. Towards Clinical Photoacoustic and Ultrasound Imaging: Probe Improvement and Real-Time Graphical User Interface. *Exp. Biol. Med.* **2020**, *245*, 321–329. [CrossRef] [PubMed]

16. Steinberg, I.; Huland, D.M.; Vermesh, O.; Frostig, H.E.; Tummers, W.S.; Gambhir, S.S. Photoacoustic Clinical Imaging. *Photoacoustics* **2019**, *14*, 77–98. [CrossRef]

17. Choi, W.; Park, E.-Y.; Jeon, S.; Kim, C. Clinical photoacoustic imaging platforms. *Biomed. Eng. Lett.* **2018**, *8*, 139–155. [CrossRef]

18. Jeon, S.; Park, E.-Y.; Choi, W.; Managuli, R.; Jong Lee, K.; Kim, C. Real-time delay-multiply-and-sum beamforming with coherence factor for in vivo clinical photoacoustic imaging of humans. *Photoacoustics* **2019**, *15*, 100136. [CrossRef]

19. Merčep, E.; Deán-Ben, X.L.; Razansky, D. Combined pulse-echo ultrasound and multispectral optoacoustic tomography with a multi-segment detector array. *IEEE Trans. Med Imaging* **2017**, *36*, 2129–2137. [CrossRef]

20. Kothapalli, S.-R.; Sonn, G.A.; Choe, J.W.; Nikoozadeh, A.; Bhuyan, A.; Park, K.K.; Cristman, P.; Fan, R.; Moini, A.; Lee, B.C.; et al. Simultaneous transrectal ultrasound and photoacoustic human prostate imaging. *Sci. Transl. Med.* **2019**, *11*, eaav2169. [CrossRef]

21. Kim, J.; Kim, Y.H.; Park, B.; Seo, H.M.; Bang, C.H.; Park, G.S.; Park, Y.M.; Rhie, J.W.; Lee, J.H.; Kim, C. Multispectral Ex Vivo Photoacoustic Imaging of Cutaneous Melanoma for Better Selection of the Excision Margin. *Br. J. Dermatol.* **2018**, *179*, 780–782. [CrossRef] [PubMed]

22. Park, B.; Bang, C.H.; Lee, C.; Han, J.H.; Choi, W.; Kim, J.; Park, G.S.; Rhie, J.W.; Lee, J.H.; Kim, C. 3D Wide-field Multispectral Photoacoustic Imaging of Human Melanomas In Vivo: A Pilot Study. *J. Eur. Acad. Dermatol. Venereol.* **2020**. [CrossRef] [PubMed]

23. Choi, W.; Oh, D.; Kim, C. Practical photoacoustic tomography: Realistic limitations and technical solutions. *J. Appl. Phys.* **2020**, *127*, 230903. [CrossRef]

24. Lee, C.; Choi, W.; Kim, J.; Kim, C. Three-dimensional clinical handheld photoacoustic/ultrasound scanner. *Photoacoustics* **2020**, *18*, 100173. [CrossRef] [PubMed]

25. Singh, M.K.A.; Sato, N.; Ichihashi, F.; Sankai, Y. Real-time improvement of LED-based photoacoustic image quality using intermittent pulse echo acquisitions. *Proc. SPIE* **2020**. [CrossRef]

26. Kim, C.; Qin, R.; Xu, J.S.; Wang, L.V.; Xu, R. Multifunctional microbubbles and nanobubbles for photoacoustic and ultrasound imaging. *J. Biomed. Opt.* **2010**, *15*, 010510–010513. [CrossRef]

27. Park, B.; Lee, K.M.; Park, S.; Yun, M.; Choi, H.-J.; Kim, J.; Lee, C.; Kim, H.; Kim, C. Deep tissue photoacoustic imaging of nickel (II) dithiolene-containing polymeric nanoparticles in the second near-infrared window. *Theranostics* **2020**, *10*, 2509. [CrossRef]

28. Park, S.; Park, G.; Kim, J.; Choi, W.; Jeong, U.; Kim, C. Bi2Se3 nanoplates for contrast-enhanced photoacoustic imaging at 1064 nm. *Nanoscale* **2018**, *10*, 20548–20558. [CrossRef]

29. Francis, K.J.; Booijink, R.; Bansal, R.; Steenbergen, W. Tomographic Ultrasound and LED-Based Photoacoustic System for Preclinical Imaging. *Sensors* **2020**, *20*, 2793. [CrossRef]

30. Singh, M.K.A. *LED-Based Photoacoustic Imaging: From Bench to Bedside*; Springer Nature: Berlin/Heidelberg, Germany, 2020.

31. Needles, A.; Heinmiller, A.; Sun, J.; Theodoropoulos, C.; Bates, D.; Hirson, D.; Yin, M.; Foster, F.S. Development and initial application of a fully integrated photoacoustic micro-ultrasound system. *IEEE Trans. Ultrason. Ferroelectr. Freq. Control* **2013**, *60*, 888–897. [CrossRef]

32. Forbrich, A.; Heinmiller, A.; Zemp, R.J. Photoacoustic imaging of lymphatic pumping. *J. Biomed. Opt.* **2017**, *22*, 106003. [CrossRef] [PubMed]

33. Lakshman, M.; Needles, A. Screening and quantification of the tumor microenvironment with micro-ultrasound and photoacoustic imaging. *Nat. Methods* **2015**, *12*, III–V. [CrossRef]

34. Paproski, R.J.; Forbrich, A.; Huynh, E.; Chen, J.; Lewis, J.D.; Zheng, G.; Zemp, R.J. Porphyrin nanodroplets: Sub-micrometer ultrasound and photoacoustic contrast imaging agents. *Small* **2016**, *12*, 371–380. [CrossRef] [PubMed]

35. Langhout, G.C.; Grootendorst, D.J.; Nieweg, O.E.; Wouters, M.W.J.M.; van der Hage, J.A.; Jose, J.; van Boven, H.; Steenbergen, W.; Manohar, S.; Ruers, T.J.M. Detection of melanoma metastases in resected human lymph nodes by noninvasive multispectral photoacoustic imaging. *Int. J. Biomed. Imaging* **2014**, *2014*. [CrossRef]

36. Harrison, T.; Ranasinghesagara, J.C.; Lu, H.; Mathewson, K.; Walsh, A.; Zemp, R.J. Combined photoacoustic and ultrasound biomicroscopy. *Opt. Express* **2009**, *17*, 22041–22046. [CrossRef]

37. Wang, Y.; Xu, D.; Yang, S.; Xing, D. Toward in vivo biopsy of melanoma based on photoacoustic and ultrasound dual imaging with an integrated detector. *Biomed. Opt. Express* **2016**, *7*, 279–286. [CrossRef]

38. Jeon, M.; Kim, J.; Kim, C. Multiplane spectroscopic whole-body photoacoustic imaging of small animals in vivo. *Med. Biol. Eng. Comput.* **2014**, *54*, 283–294. [CrossRef]

39. Cho, S.; Baik, J.; Managuli, R.; Kim, C. 3D PHOVIS: 3D photoacoustic visualization studio. *Photoacoustics* **2020**, *18*, 100168. [CrossRef]